Microscale Thermophysical Engineering, 8:101–109, 2004

ISSN: 1089-3954 print/1091-7640 online
DOI: 10.1080/10893950490445252

Taylor & Francis
Taylor & Francis Group

EXPERIMENTAL CHARACTERIZATION OF ANODE HEATING DUE TO ELECTRON FIELD EMISSION

C. T. Harris and D. G. Walker
Vanderbilt University, Department of Mechanical Engineering, Nashville, TN

T. S. Fisher
Purdue University, School of Mechanical Engineering, West Lafayette, IN

W. H. Hofmeister
Vanderbilt University, Department of Chemical Engineering, Nashville, TN

Recent advances in cold cathode field emitters have produced improvements in emission efficiency and thus enhanced the applicability of such devices. This article considers heating due to electron field emission from a polycrystalline diamond cathode. Temperature measurements from infrared thermography reveal highly localized heating due to nonuniform emission from the cathode. Power dissipation of 0.36 W produces a peak temperature increase of 12.5 K on the back surface of the water-cooled anode. Parameter estimation techniques are employed to predict the effective size of the heat source and the fraction of total power that is dissipated near hot spots. The estimates indicate effective heated radii of order 1 mm and power fractions in the range of 25% to 50%.

Keywords electron field emission, anode heating, electron beam

Significant progress has been achieved in recent years in the creation of electron field emission devices with reduced turn-on voltages and increased current density. Much of this progress is a consequence of novel materials and synthesis techniques that enable the fabrication of nanometer-scale features to produce extremely large electric-field enhancement. Applications for these new devices include electron sources for flat-panel displays, power diodes, and microwave circuit components. The large local current densities and (still) relatively large operating voltages of these devices cause substantial local heating of the anode. In the present work, anode heating due to electron emission from a polycrystalline diamond cathode is studied experimentally to determine the magnitude and localization of heating in a practical configuration.

Electron field emission has been studied for nearly the past one hundred years. Fowler and Nordheim [1] first developed a theory for the electron tunnelling mechanism

Received 1 July 2002; accepted 13 June 2003.

CVD diamond emitter samples were prepared in collaboration with the Vanderbilt Diamond Technology Program, directed by Prof. J. L. Davidson. The second author gratefully acknowledges support by the National Science Foundation's CAREER Program (CTS-9983961).

Address correspondence to T. S. Fisher, Purdue University, School of Mechanical Engineering, 1288 ME Building, West Lafayette, IN 47907-1288. E-mail: tsfisher@purdue.edu

NOMENCLATURE

d	anode thickness	r	radial coordinate
G	volumetric heat generation rate	R_0	estimated radius of heated region
I	total emission current	R_1	outer radius of anode
k	anode thermal conductivity	T	temperature
P_f	estimated power fraction in primary heated region	ΔT	temperature rise

from a planar metallic surface. Over the past several decades, Spindt-type tip emitters [2] fabricated from a variety of metallic and semiconducting materials have been studied [3, 4]. However, field emission devices have not found widespread use in practical applications due to low total current caused by strongly non-uniform emission and reliability issues involving tip erosion and degradation caused by excessive anode heating, the subject of the present work.

Recently developed carbon-based emission materials offer significant promise in addressing traditional limitations of field emission devices, even though the precise emission mechanisms remain the subject of intense scientific study [5]. Polycrystalline diamond films [6] and molded tip arrays [7] exhibit high current densities and reliable operation. Further, carbon nanotubes possess excellent field emission properties [8]. Zhu et al. [9] reported anode current densities of 4 A/cm^2 and hypothesized that current densities five to seven orders of magnitude greater are possible. In these experiments, the estimated temperature of the needle-type anode was 1980 K. Such large current and power densities require detailed understanding of heat transport in field emission devices in order to provide adequate cooling solutions.

The present work reports results of experiments conducted to characterize localized anode heating caused by field emission in a thermally controlled environment. The results elucidate issues involving non-uniform electron emission from the cathode, temporal changes in emission location and heating, and the extent of heat localization on the anode. The following section describes the experimental specimen and setup. Subsequent sections present results and conclusions from the work.

EXPERIMENTAL SETUP

A polycrystalline diamond film cathode was used in the present work. The film was grown with molded tip features by plasma-enhanced chemical vapor deposition and post-growth procedures described by Kang et al. [10]. Figure 1 contains an SEM image of the cathode, which consists of an array of molded pyramids of 12 μm base dimension and pitch. The tip radii of these types of emitters has been measured to be of the order of 10 nm [7]. The diamond film was brazed to a 100 μm-thick planar molybdenum substrate to provide electrical contact and film planarity.

Annular Al_2O_3 rings provided a gap of 250 μm between the diamond-tip sample and the 250 μm-thick stainless steel anode. An aluminum housing, coupled with Al_2O_3 spacers for electrical isolation, rigidly supported both the cathode and anode. Two copper flanges integrated with tube-pass heat exchangers were mounted to the aluminum housing.

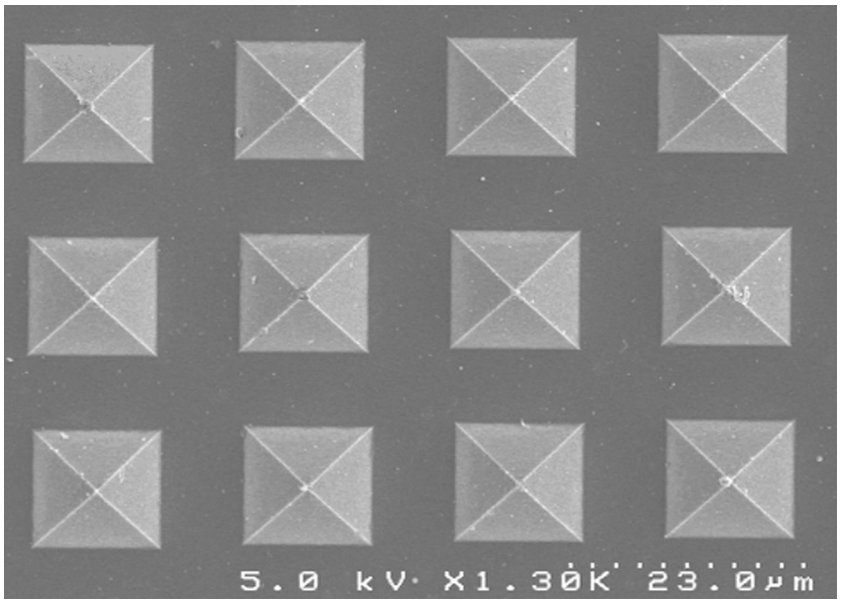

Figure 1. SEM image (plan view) of the diamond-tip array cathode. The tip array extends over a 1 cm square at 12 μm pitch. The base dimension of each pyramid is 12 μm.

A constant temperature bath maintained thermal control over the experimental apparatus by pumping water through heat exchangers.

Figure 2 contains a schematic of the experimental rig's electrical layout. A high-voltage power supply placed a constant bias across the device to achieve the desired current. A 1 MΩ, high-power shunt resistor was employed to avoid current spikes and thus prevent device shorting. A multimeter placed in series on the low-voltage side recorded emission current, and another multimeter in parallel with the power supply recorded raw voltage. The experimental rig was mounted inside a high-vacuum system operating at a typical working pressure of 1×10^{-8} torr. Anode surface temperatures were measured by an Flir SC300 IR camera mounted on top of the vacuum system. The camera viewed the anode through a germanium viewport, which allowed the proper transmittance of electromagnetic radiation [11]. The anode's back surface was coated with a flat black paint to provide a uniform viewing surface of known emissivity.

RESULTS AND DISCUSSION

To ensure that the observed current was in fact due to field emission, the current-voltage behavior of the device was first characterized. The measured current as a function of voltage is shown in Figure 3. The results indicate the presence of field emission, as evidenced by the linearity of the inset graph [3], with a turn-on voltage less than 8 V/μm.

To assess overall thermal performance, the maximum observed temperature on the back side of the anode was chosen as a general thermal metric. Figure 4 illustrates this peak temperature as a function of input electrical power (i.e., voltage $\times$ current). Data points in the figure represent averages over a 30-s period at each power setting. Error bars

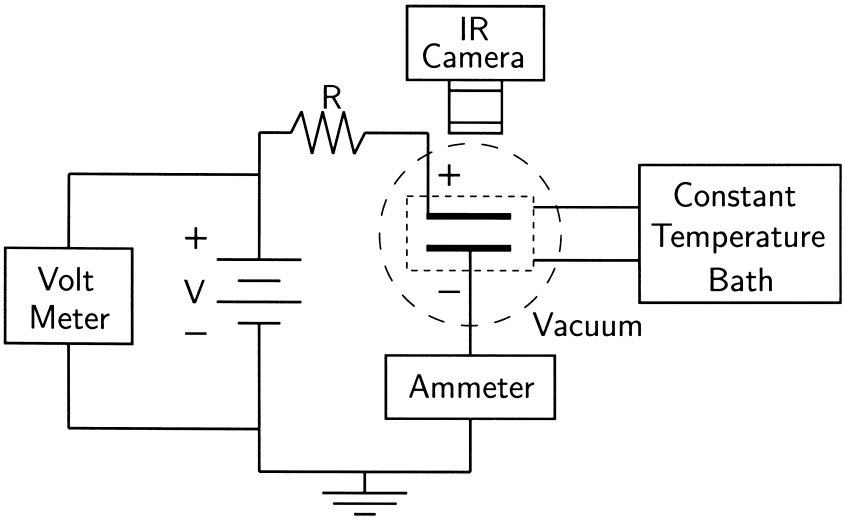

Figure 2. Schematic representation of testing system. Voltmeter and ammeter report voltage and current. IR camera captures anode surface temperatures. Constant temperature bath maintains thermal control of the system. Anode is labeled by positive (+) voltage bias. Cathode is labelled by negative (−) voltage bias.

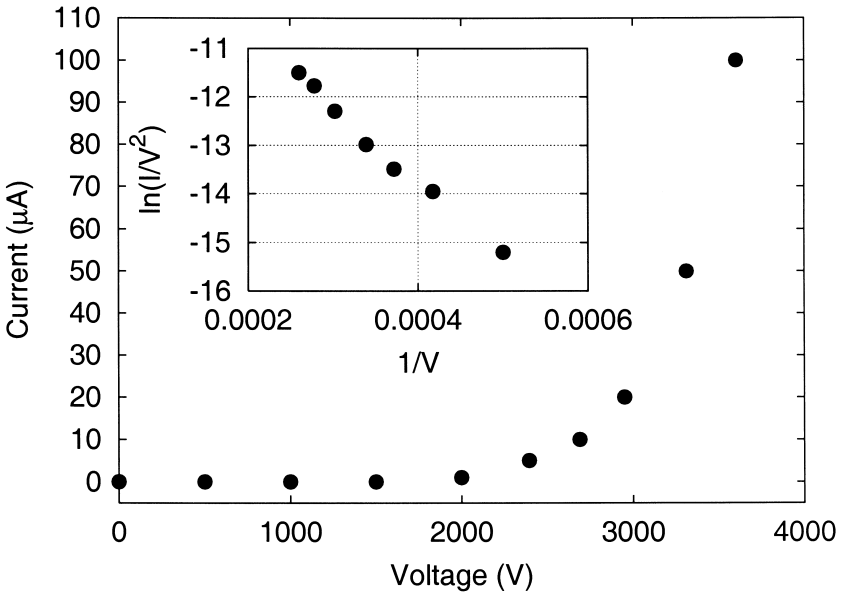

Figure 3. Current-voltage behavior of 12 μm diamond-tip array. Cathode-to-anode distance = 250 μm. Inset shows the associated Fowler-Nordheim plot for the 12 μm diamond-tip arrays.

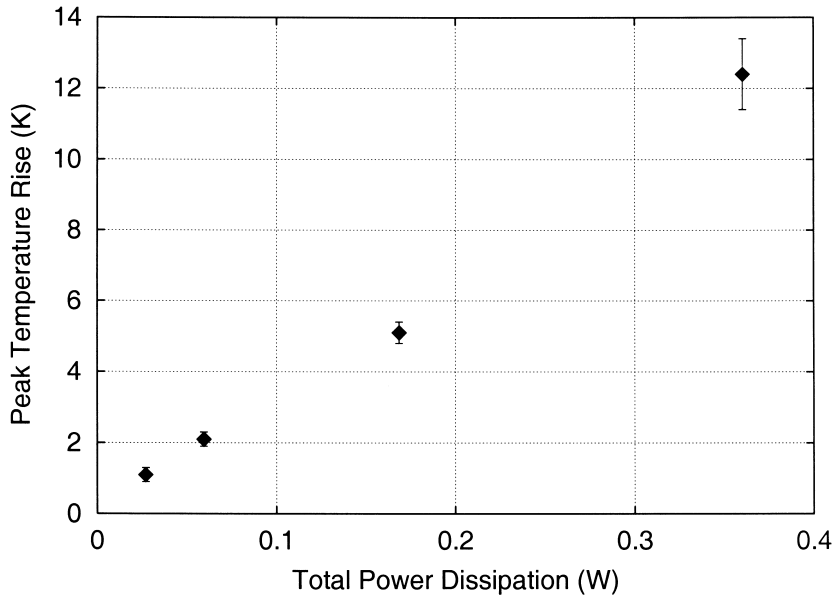

Figure 4. Peak anode temperature rise as a function of total power dissipation. Peak temperature rise defined as highest anode temperature recorded by IR imaging relative to the boundary temperature.

indicate the variation of the peak temperature difference, recorded every 1 s, over this period. The temperature-power relationship is nearly linear; however, the data indicate a slight positive curvature. This observation is consistent with later observations of localized emission from the cathode. Such non-uniformity favors increased current from dominant emission sites as voltage increases due to the exponential nature of field emission (see Fig. 3). Thus, as voltage and power increase, more energy is dissipated from the dominant emission sites, and the associated temperature metric increases commensurately. The figure also reveals increasing temperature variation with increasing power due to the fluctuating nature of the electron emission at larger currents.

Localized heating was evaluated through interrogation of the infrared thermal images. Numerous thermal images were recorded at each current and voltage condition. In some cases, the location(s) of hot spots on the anode were observed to shift with time and then became stationary. Steady-state thermal images, such as that shown in Figure 5 with a total power dissipation of 0.36 W, were recorded to reveal the full temperature field of the anode. The location of peak temperature occurs near the center of the image. The temperature contours also reveal a region of heating below the peak that suggests the presence of lower emission currents from other parts of the cathode.

Two lines, denoted as "2a" and "2b" in Figure 5, are used to quantify radial temperature profiles originating at the location of peak temperature. Similarly, four such lines were used to characterize temperature distributions for experiments with 0.17 W total power dissipation. These lines were used to estimate simultaneously the radius R_0 of the primary heated region and the fraction P_f of total power that is dissipated in the peak temperature region.

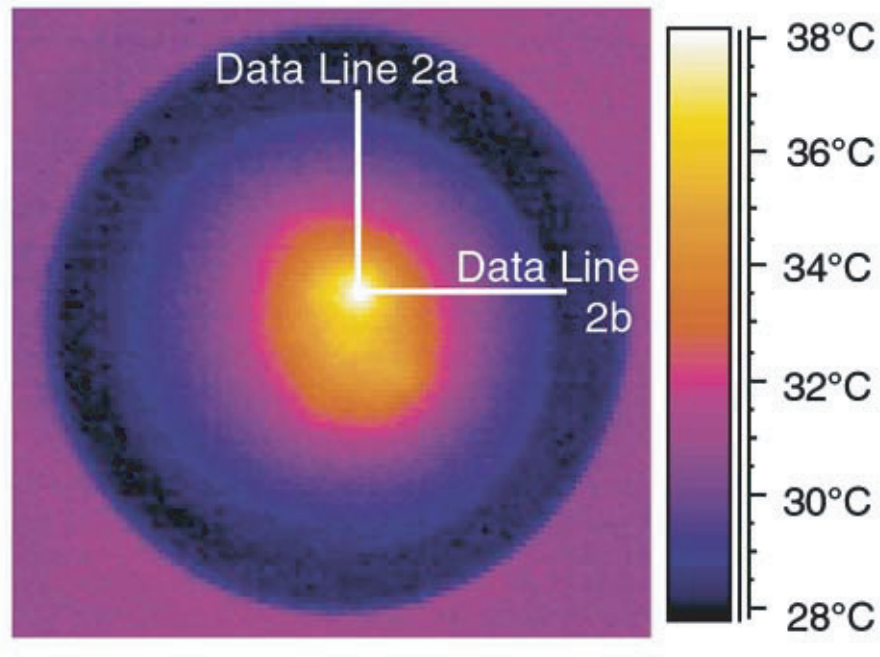

Figure 5. Infrared camera image of the anode's top surface. Labels show the data lines used for temperature measurement. Temperature scale displays the relative surface temperatures on the anode.

To estimate R_0 and P_f, a one-dimensional radial heat conduction model with azimuthal symmetry was employed to provide temperature predictions based on volumetric heating. The anode thickness is $d = 250$ μm, and radiation heat transfer from the back (visible) side of the anode can be neglected under the experimental conditions. Therefore, heat transfer in the axial direction was ignored. Under these assumptions, the heat generation rate can be expressed in terms of the power fraction (P_f), the electrical energy in the beam (IV), and the volume in which energy is deposited:

$$G = P_f \frac{IV}{\pi R_0^2 d} \tag{1}$$

The far-field boundary at $r = R_1$ is assumed to be at the temperature of the water-cooled ring surrounding the anode. The closed-form temperature solution is

$$T(r) - T(R_1) = \begin{cases} P_f \dfrac{IV}{2\pi kd}\left[\dfrac{1}{2} - \ln\dfrac{R_0}{R_1} - \dfrac{r^2}{2R_0^2}\right] & r < R_0 \\ -P_f \dfrac{IV}{2\pi kd} \ln\dfrac{r}{R_1} & r \geq R_0 \end{cases} \tag{2}$$

Two-parameter estimation was performed using least-squares minimization of the difference between measured and calculated temperatures. Because a closed-form analytic

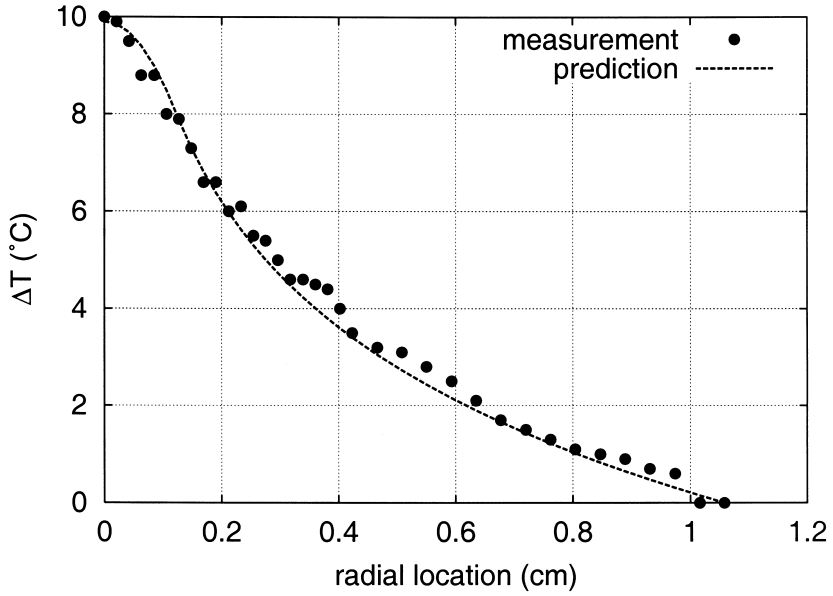

Figure 6. Temperature as a function of radius with experimental measurements (points) and calculated estimates (line) along line 2a (see Fig. 5) for case of 0.36 W total power dissipation.

solution exists, parameter sensitivities (i.e., derivatives of temperature with respect to unknown parameters) were evaluated in closed form and shown to be uncorrelated. Measured temperatures along lines extending radially outward from the center of the spot were used to compare to calculated temperatures from the conduction model. Because the spot is not axially symmetric and the effects of multiple heated regions overlap to some extent, data in several directions were used to predict the parameters. Also, because the estimate for heated beam radius is more sensitive to data near the highest temperature, the data were weighted by the factor $(r + 0.01)^{-1}$, with r measured in centimeters.

Measured and predicted radial temperature profiles are shown in Figure 6 for the case of 0.36 W total power dissipation. The predicted profile is based on a heated radius of $R_0 = 0.121$ cm and a power fraction of $P_f = 24.7\%$. Good agreement exists between the two results over a 1-cm radius.

Estimates of beam radius R_0 and power fraction P_f are provided in Table 1 for experiments involving two total power dissipations, 0.17 W and 0.36 W. The former experiment involved a nominal field of 13.48 V/μm resulting in a total current of 50 μA, and the latter involved a field of 14.4 V/μm resulting in a total current of 100 μA. For both cases, 95% confidence intervals are provided with the estimates for beam radius and power fraction and indicate reasonably moderate uncertainties of these parameters.

The predicted heated radii, typically of order 0.1 cm, are significantly larger than would be expected for a beam from a single emitter, while the predicted power fractions are somewhat lower than expected. With a vacuum gap of 250 μm, the spreading radius from a single emitter would likely not exceed 50 μm. A possible explanation for the predictions of large R_0 is that the primary heated zone is caused by emission from a group of emitter tips, as opposed to a single tip emitter. Further, axial heat conduction

Table 1. Estimates of beam radius R_0 and beam power fraction P_f and associated 95% confidence intervals for two experiments. Each experiment contains data from several radial lines extending 1.1 cm from the location of peak temperature.

Test	Total power (W)	Line no.	R_0 (cm)	P_f (%)	Temperature change (K)
1	0.17	1a	0.130 ± 0.057	27.6 ± 3.0	4.6
		1b	0.494 ± 0.038	43.4 ± 2.8	5.4
		1c	0.121 ± 0.024	25.6 ± 1.0	5.0
		1d	0.239 ± 0.015	35.4 ± 1.0	5.0
2	0.36	2a	0.121 ± 0.021	24.7 ± 1.9	10.0
		2b	0.112 ± 0.024	23.7 ± 1.3	9.9

from the heated side to the back (i.e., viewed) side and its effect on the temperature distribution were not included in the model but may be significant due to the very large local heat fluxes present on the heated surface.

CONCLUSIONS

This work has presented detailed experimental results of localized heating due to electron field emission. The results show that peak anode temperatures increase slightly non-linearly with total power (see Fig. 4); thus, field emission devices might not be amenable to a single thermal resistance metric such as those typically used for solid-state devices.

In general, the observed peak temperatures are substantially larger than might be expected for the low power conditions of the experiments and the relatively large size of the emitter (1 cm $\times$ 1 cm). However, the localized (and sometimes transient) nature of field emission causes the formation of local hot spots on the anode. Explanations for this localization of current and heating include nonuniformity of the cathode surface, micro- or nano-structural variation within the cathode, and lack of perfectly planar separation between the anode and cathode. These issues have perplexed researchers since the beginning of field emission research and will likely continue into the future. Given much recent progress in the development of new field emission materials and applications, thermal analysis and management of these devices will remain a significant and important challenge.

REFERENCES

1. R. H. Fowler and L. W. Nordheim, Field Emission from Metallic Surfaces, *Proceedings of the Royal Society A*, vol. 119, pp. 173–181, 1928.
2. C. A. Spindt, A Thin Film Field Emission Cathode, *Journal of Applied Physics*, vol. 39, pp. 3504–3505, 1968.
3. I. Brodie and P. R. Schwoebel, Vacuum Microelectronic Devices, *Proceedings of the IEEE*, vol. 82, pp. 1006–1018, 1994.
4. J. A. Nation, L. Schachter, F. M. Mako, L. K. Len, W. Peter, C.-M. Tang, and T. Srinivasan-Rao, Advances in Cold Cathode Physics and Technology, *Proceedings of the IEEE*, vol. 87, pp. 865–889, 1999.

5. R. G. Forbes, Low-Macroscopic-Field Electron Emission from Carbon Films and Other Electrically Nanostructured Heterogeneous Materials: Hypothesis about Emission Mechanism, *Solid-State Electronics*, vol. 45, pp. 779–808, 2001.
6. F. A. M. Koch, J. M. Garguilo, and R. J. Nemanich, Imaging Electron Emission from Diamond Film Surfaces: N-Doped Diamond vs. Nanostructured Diamond, *Diamond and Related Materials*, vol. 10, no. 9–10, pp. 1714–1718, 2001.
7. W. P. Kang, T. S. Fisher, and J. L. Davidson, Diamond Microemitters—The New Frontier of Electron Field Emission and Beyond, *New Diamond and Frontier Carbon Technology*, vol. 11, pp. 129–146, 2001.
8. J. M. Bonard, H. Kind, T. Stockli, and L. A. Nilsson, Field Emission from Carbon Nanotubes: The First Five Years, *Solid-State Electronics*, vol. 45, no. 6, pp. 893–914, 2001.
9. W. Zhu, C. Bower, G. P. Kochanski, and S. Jin, Field Emission Properties of Diamond and Carbon Nanotubes, *Diamond and Related Materials*, vol. 10, pp. 1709–1713, 2001.
10. W. P. Kang, J. L. Davidson, M. Howell, B. Bhuva, D. L. Kinser, D. V. Kerns, Q. Li, and J. F. Xu, Micropatterned Polycrystalline Diamond Field Emitter Vacuum Diode Arrays, *Journal of Vacuum Sciences and Technologies B*, vol. 14, pp. 2068–2071, 1996.
11. G. D. Nutter, Radiation Thermometry—The Measurement Problem, Applications of Radiation Thermometry, *ASTM*, STP 895, J. C. Richmond and D. P. Dewitt, Eds., American Society for Testing and Materials, Philadelphia, 1985.